

Stress path dependent hydromechanical behaviour of heterogeneous carbonate rock

N. Gland^{1,a}, J. Dautriat^{1,2}, A. Dimanov², and J. Raphanel²

¹ I.F.P., 1-4 av. de Bois Préau, 92852, Rueil-Malmaison, Cedex, France

² Laboratoire de Mécanique des Solides, UMR 7649, Ecole Polytechnique, 91128 Palaiseau, France

Abstract. The influence of stress paths, representative of reservoir conditions, on the hydromechanical behavior of a moderately heterogeneous carbonate has been investigated. Multiscale structural heterogeneities, common for instance in carbonate rocks, can strongly alter the mechanical response and significantly influence the evolution of flow properties with stress. Using a triaxial cell, the permeability evolutions during compression and the effects of brittle (fracture) and plastic (pore collapse) deformations at yield, were measured. A strong scattering was observed on the mechanical response both in term of compressibility and failure threshold. Using the porosity scaling predicted by an adapted effective medium theory (based on crack growth under Hertzian contact), we have rescaled the critical pressures by the normalized porosity deviation. This procedure reduces efficiently the scattering, revealing in the framework of proportional stress path loading, a linear relation between the critical pressures and the stress path parameter through all the deformation regimes. It leads to a new formulation for the critical state envelope in the 'mean stress, deviatoric stress' diagram. The attractive feature of this new yield envelope formulation relies on the fact that only the two most common different mechanical tests 'Uniaxial Compression' and 'Hydrostatic Compression', are needed to define entirely the yield envelope. Volumic strains and normalized permeabilities are finally mapped in the stresses diagram and correlated.

1. Introduction

Oil field production leads to change in reservoir pore pressure, resulting in modifications of effective stresses acting on the reservoir; it induces both elastic and inelastic deformations of rocks and potentially compaction at the reservoir scale. These deformations of the porous structures modify the transport properties, and thus the production efficiency [1]. Several extensive experimental studies have investigated the dependency of rock permeability on effective pressure, during the brittle regime and cataclastic flow of sandstones [2,3,4,5,6]. In carbonates, the microstructural control of failure mechanisms is more complex than in sandstones and remains an extended matter of research [7]. The macroscopic yielding seems to be controlled by both crystal plasticity and grains microcracking. On low porosity limestones, mechanical data have been interpreted on the basis of a crystal plasticity model [8]. Since for more porous carbonates, microcracking becomes the major damage mechanism, such model is not appropriate [9,10] and others effective media models [11,12] based on microcracks growths theory are tested [13]. Following a similar approach, we highlight the effects of heterogeneities on the mechanical response of bioclastic carbonates.

^a E-mail : nicolas.gland@ifp.fr

2. Microstructural description and heterogeneities

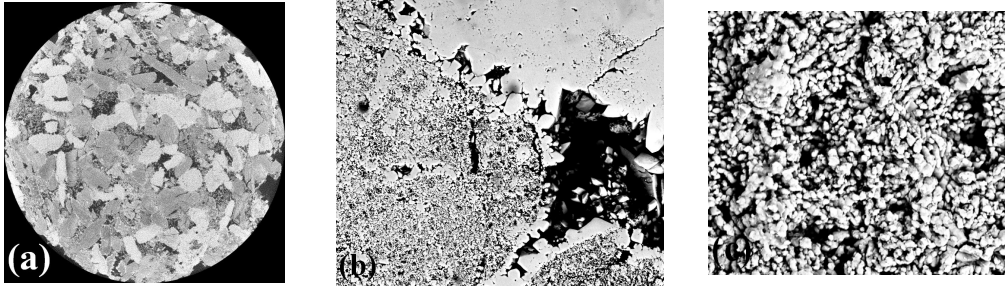


Fig. 1. Microstructure of Estailades Carbonate: (a) μ -CT image of a mini-plug; SEM (BSE) images of: (b) triple junction: microporous and dense grains and macropore; (c) zoom in a microporous grain.

The Estailades carbonate is composed almost exclusively of calcite micro-grains of size ranging from $1\mu\text{m}$ to $10\mu\text{m}$ (Fig.1(c)). Nevertheless, this carbonate presents structural heterogeneities at different scales [14]. The Figure 1(a) shows that the micro-grains of calcite gather in two kinds of aggregates of size less than $500\mu\text{m}$, some very dense (Fig.1(b) top), and the others microporous (Fig.1(b) left). A larger porosity is also present between the aggregates (Fig.1(b) right). These aggregates characterize the elementary micro-heterogeneity. This double porosity structure is confirmed by Hg Porosimetry and NMR T2 distributions [15].

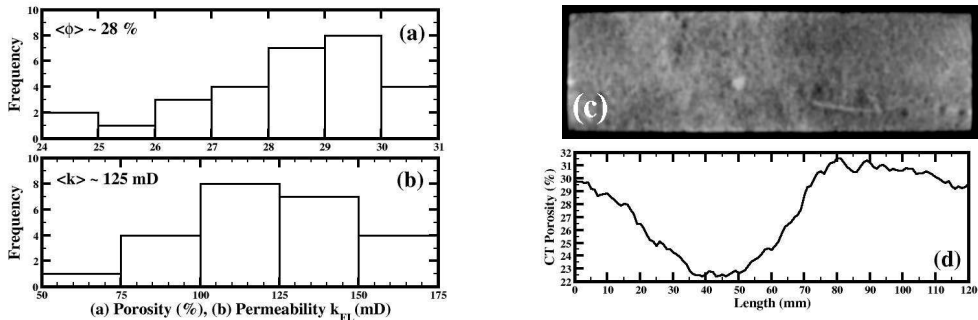


Fig. 2. Petrophysical characteristics of the Estailades carbonate: (a) porosity and (b) permeability histograms of ~ 30 samples cored in a single bloc; to illustrate the heterogeneity, CT-RX (c) density map and (d) porosity profile of a very heterogeneous sample.

As illustrated on the Figure 2 with a particularly heterogeneous sample, the spatial distribution of the aggregates (c) can lead to local variations of porosity (d) and thus to a meso-heterogeneity. For the present hydromechanical study, homogeneous and moderately heterogeneous samples were selected. At sample scale, the porosity variation from one sample to another (Fig.2(a)), between 24% and 31%, traduces the macro-heterogeneity. These heterogeneities, at different scales, lead to significant permeability fluctuations from 50mD to 175mD (Fig.2(b)). As a result, no correlation between porosity and permeability can be really identified.

3. Stress-path dependent mechanical properties

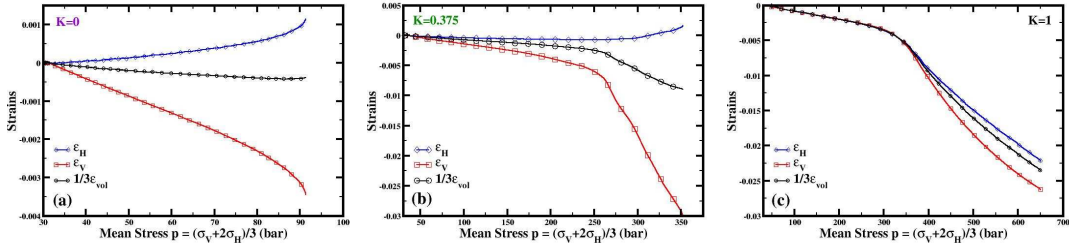


Fig. 3. Mean stress - strains (vertical in red, horizontal in blue, volumic in black) curves, typical of the three deformation regimes: (a) brittle; (b) transitional with shear enhanced compaction and (c) purely compactant.

In this study, the samples are compressed triaxially and continuously, following different stress paths, representative of reservoir conditions [16], defined by the parameter:

$$K = \frac{\Delta\sigma_H}{\Delta\sigma_V}, \quad (1)$$

with $\Delta\sigma_H$ and $\Delta\sigma_V$, the horizontal and vertical stresses increments. Our triaxial cell [17] operates for confining pressure and vertical stress up to 690bar. To insure the sealing of the elastomer sleeve on the sample, for permeability measurements, an initial confinement of $p_c=30$ bar is required. Seven sets of three samples (dimensions: 80mm height, 40mm diameter) were submitted to each following stress path $K=0$, $K=0.125$, $K=0.25$, $K=0.375$, $K=0.5$, $K=0.75$ and $K=1$. The axial loading rate $\Delta\sigma_V$ was set to 1 bar/min for all K and the radial loading rate $\Delta\sigma_H$ was set according to K . The mechanical response of the samples is obviously dependent of the selected stress path, but for a given loading path, the response is also tightly linked to the degree of heterogeneity between the different tested samples. These aspects are detailed below.

Brittle Regime. For $K=0$ and $K=0.125$, the damage is localized and results at a threshold pressure p^* in a brittle failure, either by two conjugated fractures, or by a single oblique fracture, whose inclination with respect to the vertical stress direction depends on K , but also on the structural heterogeneities.

Localized Compactant Regime. For $K=0.25$ and $K=0.375$, the regime is transitional, or semi-brittle. The elastic regime shows limited compaction up to the critical pressure threshold p^* , where the apparition of a localized shear band induces a macroscopic vertical compaction. The pressure rise stabilizes this compaction, up to a second critical pressure threshold p^{**} , which define the cataclastic dilatant regime. As observed by others authors [8], this regime does not show any localization, but results in deformed barrel-shaped samples. Under loading, we observe an important reduction of porosity, whose evolution corresponds to the bulk deformation. But during unloading, we also observe the opening of a new porosity, linked to diffuse microcracking.

Diffuse Compactant Regime. For $K=0.75$ and $K=1$, above p^* , the deformation regime is purely compactant (see ϵ_v in Fig.3(c)) with the collapse of the macro-porosity network [15], initially present between the different aggregates (Fig.1(b)). This macro-pores collapse corresponds in the Hg porosimetry distribution to the shift from $10\mu\text{m}$ to $3\mu\text{m}$ of the capillary macro-throat sizes. While, homogeneous samples compact homogeneously, CT porosity profiles show that for heterogeneous samples, the regions displaying the most important compaction (i.e. porosity reduction) correspond to the initially more porous parts.

4. Renormalisation of critical pressures

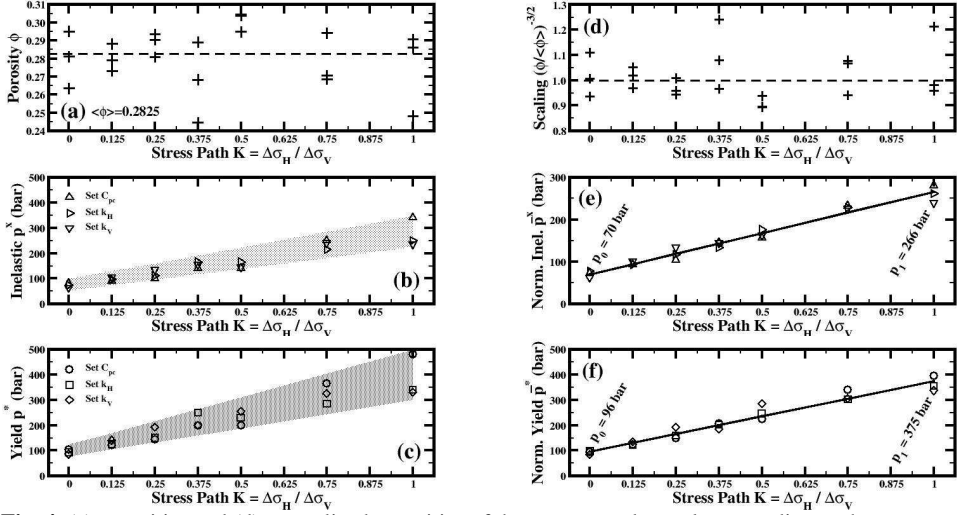


Fig. 4. (a) porosities and (d) normalized porosities of the compressed samples according to the stress path parameter K ; corresponding (b) inelastic mean stress p^X (triangles) and (c) yield mean stress p^* (others symbols); scattering prevents identification of $p(K)$ relations (see grey regions); (e, f) mean stress normalisation by scaling parameter (d) reduces the scattering and allows to identify linear $p(K)$ relations.

Our data of p^X and p^* , presented in Figure 4(b,c), show that for a given stress path K , it exists an important scattering; in the worst case (for instance for $K=1$), a difference of more than 100 bar between the two extreme values can be observed; it clearly prevents any meaningful elliptic description in (p, q) stresses space, either for the onset of inelasticity or for the yield. While, it is common to normalize p and q by the value p_1^* (for $K=1$), which determination is impossible here, due to the scattering. In addition, we notice in Figures 4(a,b,c), that the greatest variations of critical mean pressures correspond to the samples presenting the biggest variations of porosity. The scattering of the mechanical data is therefore correlated to the strong heterogeneity of the porous structure of the studied carbonate. To reduce its impact, we have applied an effective media model [12], which combines the theory of Hertzian contact, the yield mechanics (microcrack growth) and an effective granular medium model [18]. This model links in particular the critical pore collapse pressure p^* (in hydrostatic condition) to the porosity ϕ and the grain size d_g through a power law scaling with an exponent $-3/2$:

$$p^* \propto (d_g \phi)^{-3/2}, \quad (2)$$

By considering the aggregate size as constant, we have performed a normalisation of the pressures p^X and p^* values (Fig.4(e,f)) by the normalized porosities of each sample (Fig.4(d)) as:

$$\frac{-}{p} \rightarrow p^* / \left(\frac{\phi}{\langle\phi\rangle} \right)^{-3/2}, \quad (3)$$

This normalization procedure reduces very significantly the scattering of the data and linear relations emerge clearly between the critical mean pressures and the stress path parameter K (Fig.4(e,f)). The slope of this straight line corresponds to the difference between the critical mean pressures p_1^* for a hydrostatic compression test ($K=1$) and p_0^* for an uniaxial compression test ($K=0$). Thus, the critical pressure p^* for any stress path parameter K can be obtained by:

$$p_K^* = (p_1^* - p_0^*)K + p_0^*, \quad (4)$$

5. Inelastic and yield caps

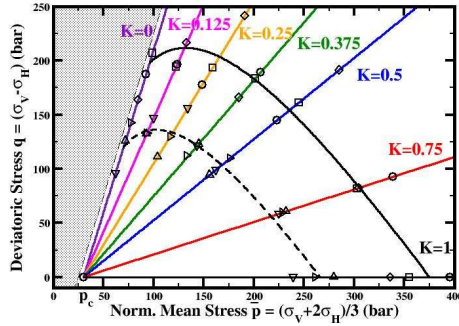


Fig. 5. Inelastic and yield caps (dashed and solid line) after mean stress normalization, obtained from the linear $p(K)$ relations (see Fig. 6.(e) and (f)).

The transposition of the linear relation (4) into the stresses space (p, q) establishes a new yield model, depending only on K . Since, for a given K , the vertical stress σ_V and horizontal stress σ_H verify:

$$\sigma_H = K(\sigma_V - p_c) + p_c, \quad (5)$$

with p_c , the initial confining pressure. For any proportional stress path (and thus damage regime), the deviatoric stress q is related to the mean pressure p by:

$$q = 3 \frac{(1-K)}{(1+2K)} (p - p_c), \quad (6)$$

Combining equations (4) and (6), we obtain a new expression for the yield envelope, as illustrated in the Figure 5:

$$q^* = 3 \frac{(p_1^* - p)(p - p_c)}{(p_1^* - 3p_0^* + 2p)}, \quad (7)$$

The Figure 5 shows a good agreement of the inelastic (dashed line) and yield (solid line) envelopes defined by equation (7) with the experimental critical pressures normalized according to equation (3). Above ~ 250 bar of mean pressure, this new formulation underlines the hydrostatic component of the stress tensor on the damage mechanisms; indeed, between ~ 250 bar and $p_1^* = 375$ bar, the cap geometry tends towards a certain linearity $q^* \propto -p^*$, which is coherent with the observations of the compactant behaviour at yield for $K > 0.5$. For smaller mean pressures, the contribution of the deviatoric component is more important, in agreement with the mechanisms of shear induced compaction and brittle failure. Contrary to the classical elliptic approach, this new envelope formulation does not require any fitting parameter. Only two kinds of mechanical test, one at constant confining pressure ($K=0$ for instance), the other in hydrostatic condition, are needed to describe fully the yield envelope. Yet, due to the carbonate heterogeneity, several tests for these two stress paths should be performed to average the scattering.

6. Cap parametrization

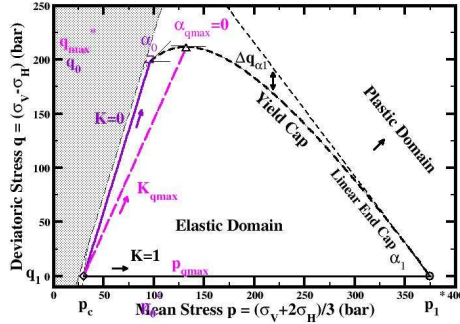


Fig. 6. Cap parametrization: local slopes at ends, apex and departure point from linearity (see Eq. 7 to 14).

Characteristic features of the proposed cap model in the stresses space (p, q) (Eq. 7) are presented on the Figure 6; those parameters can be obtained directly from the two experiments $K=0$ and $K=1$.

The local slope of the cap α being given by:

$$\alpha = 3 \left[\frac{(p_1^* + p_c - 2p)}{(p_1^* - 3p_0^* + 2p)} - 2 \frac{(p_1^* - p)(p - p_c)}{(p_1^* - 3p_0^* + 2p)^2} \right], \quad (8)$$

the local slopes at p_0^* and p_1^* :

$$\alpha_0 = 3 \left[1 - 3 \frac{(p_0^* - p_c)}{(p_1^* - p_0^*)} \right], \quad (9)$$

$$\alpha_1 = - \frac{(p_1^* - p_c)}{(p_1^* - p_0^*)}, \quad (10)$$

are respectively $\alpha_0=0.87$ and $\alpha_1=-1.23$ for $p_c=30$ bar, $p_0^*=96$ bar and $p_1^*=375$ bar.

The apex of the cap, characterized by $\alpha_{q_{\max}}=0$ (q^* is maximum), corresponds to the mean pressure:

$$p_{q_{\max}}^* = \frac{1}{2} \left(\sqrt{3} \sqrt{p_1^{*2} + 3p_0^{*2} - 4p_1^*p_0^* + 3p_c(p_1^* - p_0^*)} + 3p_0^* - p_1^* \right), \quad (11)$$

Equation (7) is then used to obtain the corresponding q_{\max}^* and the stress path parameter $K_{q_{\max}}^*$ intersecting the cap at its apex is obtained by combination of equations (6) and (7):

$$K_{q_{\max}}^* = \frac{\left(3p_{q_{\max}}^* - 3p_c - q_{\max}^* \right)}{\left(3p_{q_{\max}}^* - 3p_c + 2q_{\max}^* \right)}. \quad (12)$$

One obtains $p_{q_{\max}}^* = 132$ bar, $q_{\max}^* = 212$ bar and $K_{q_{\max}}^* = 0.13$.

The departure from linearity of the cap at high effective pressure in the vicinity of p_1^* , can be quantified by the normalized gap between the straight line of slope α_1 passing p_1^* and the the cap $q^*(p)$ defined by equation (7):

$$\Delta q_{\alpha_1} = 1 - \frac{q_{Eq.7}^*}{\alpha_1 \cdot (p - p_1^*)}. \quad (13)$$

The mean pressure corresponding to the linearity deviation criterion $\Delta q_{\alpha 1}$ is:

$$p_{\Delta q_{\alpha 1}} = \frac{(1 - \Delta q_{\alpha 1})(p_1^{*2} - 3p_1^*p_0^*) + \Delta q_{\alpha 1}p_c(p_1^* - 3p_0^*) + 2p_cp_1^*}{2\Delta q_{\alpha 1}(p_1^* - p_c) + (p_1^* - 3p_0^* + p_c)}, \quad (14)$$

and significant deviation $\Delta q_{\alpha 1} = 10\%$ is thus reached for $p_{\Delta q_{\alpha 1}} = 241$ bar.

7. Stress-path dependent hydraulic properties

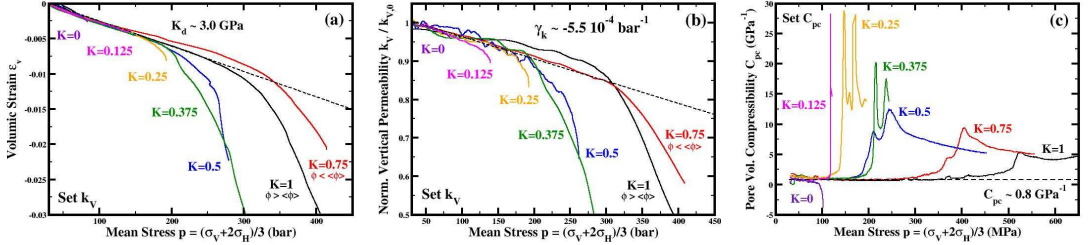


Fig. 7. (a) volumic strain, (b) vertical permeability and (c) pore volume compressibility evolutions, as a function of the mean stress, according to the seven investigated stress paths; (a,b) Same data set and (c) Other data set.

We investigate also the permeability and pore compressibility evolutions during the different loading paths. Initially, the samples are saturated with brine (30g/L NaCl). For the permeability, the flow rate is set at 0.1 mL/min and the differential pressure is measured, while the pore pressure is maintained at $p_p=10$ bar by a back pressure regulator. To measure the pore volume compressibility, the drained volume is monitored by a digital volumeter, while the pore pressure is maintained at $p_p=10$ bar by a gas buffer. In the linear deformation regime (Fig.7(a)), the permeability evolution (Fig.7(b)) is linear and pretty independent of the stress path; the average permeability reduction coefficient γ_{kv} is $\sim 5.5\%$ for 100bar of mean pressure increment. In the stresses space (p, q) , we observe that the permeability evolution is controlled essentially by the mean effective pressure, as shown by the vertical iso-permeability lines (Fig.8(b)). In the linear deformation regime, the pore volume compressibility (Fig.7(c)) is constant and also independent of the stress path with a mean value of $C_{pc} \sim 0.8 \text{ GPa}^{-1}$. Above the inelastic threshold, the permeability evolutions diverge. At high mean stress, we observe a good correlation for all stress paths between the volumic strain and the vertical permeability evolution (Fig.8); heterogeneity influence is also highlighted by the inversion of the curves between the stress paths $K=0.75$ and $K=1$ (Fig.7(a,b)). The inflection of the iso-permeability lines at low mean pressure highlights the influence of deviatoric stress on the permeability evolutions. At high pressure, for stress path $K > 0.5$, in the plastic deformation regime, the carbonate tends to follow a pore volume compressibility $C_{pc} \sim 4 \text{ GPa}^{-1}$.

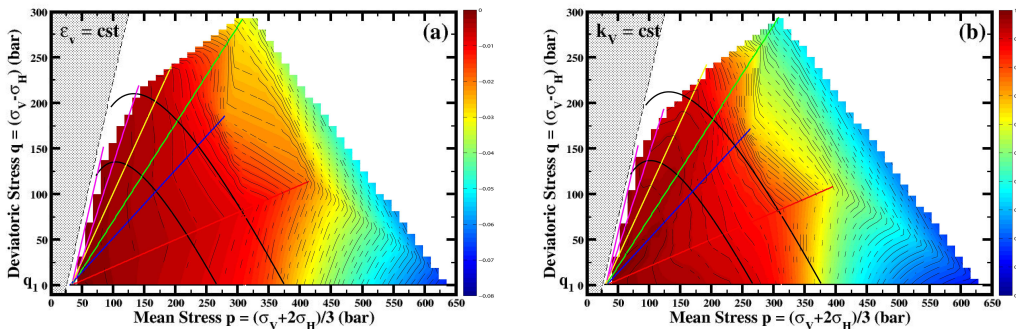


Fig. 8. (a) Iso-volumic strain and iso-vertical permeability maps, calculated by linear interpolation of the first data set of seven stress-paths compression experiments (See Fig. 7(a,b)).

8. Conclusion

We have observed the different damage modes and the impacts of the microstructural heterogeneities during hydromechanical compaction tests of carbonate samples loaded according to different stress paths. The stress path parameter K is the main parameter controlling the deformation regime and the permeabilities evolution. However, in the intermediate regimes, different samples submitted to a same K can show significantly different responses, due to their heterogeneities of porous structure. This variability leads to a strong scattering of the data in terms of critical pressures, which makes the fitting of a yield envelope in the stresses space problematic. Relying on a yield model of effective media, we propose a normalization of the critical pressures by the normalized porosities of the different samples, which reduces significantly the scattering and allows to derive of a new expression for the inelastic and yield envelopes, without any fitting parameter (in opposition to the classical elliptical formulation). The mechanical data obtained on the Estailades carbonate agree quite better with this envelope shape. Its elaboration is easy to carry out since it necessitates only two kinds of classical mechanical tests, one at constant confining pressure (i.e. $K=0$), and another one, in hydrostatic conditions (i.e. $K=1$).

References

1. Schutjens, P.M.T.M. and De Ruig, H., Phys. Chem. Earth (A), **22** (1997).
2. David, C., Wong, T.F., Zhu, W.L. and Zhang, J., Pure & Appl. Geophys., **143** (1994).
3. Zhu, W.L. and Wong, T.F., J. Geophys. Res., **102** (1997).
4. Wong, T.F., David, C. and Zhu, W., J. Geophys. Res., **102** (1997).
5. Keaney, G.M.J., Meredith, P.G. and Murrell, S.A.F., SPE, **47265** (1998).
6. Heiland, J. and Raab S., Phys. Chem Earth A, **26** (2001).
7. Yale, D.P. and Crawford, B.R., SPE Int. Symp. Rock Mech., **47582** (1998).
8. Baud, P., Zhu, W. and Wong, T.F., J. Geophys. Res., **105** (2000).
9. Vajdova, V., Baud, P. and Wong, T. F., J. Geophys. Res., **109** (2004).
10. Baud, P, Vinciguerra, S., David, C., Cavallo, A., Walker, E. and Reuschle, R., Pure & Appl. Geophys., **166** (2009).
11. Sammis, C.G., and Ashby, M.F., Acta Metall. **34** (1986).
12. Zhang, J., Wong, T.F. and Davis, D.M., J. Geophys. Res., **95** (1990).
13. Zhu, W., Baud, P. and Wong, T.F., J. Geophys. Res., **In Press**, (2010).
14. Dautriat, J., Bornert, M., Gland, N., Dimanov, A., Raphanel, J. And Vizika, O., Proc. Symp. Soc. Core Analysts, **22** (2009).
15. Dautriat, J., Gland, N., Youssef, S., Rosenberg, E., Bekri, S. and Vizika, O., SPE Res. Eval. & Eng., **12** (2009).
16. Rhett, D.W., and Teufel, L. W., Proc. U.S. Symp. on Rock Mech. (1992).
17. Dautriat, J., Gland, N., Guelard, J., Dimanov, A. and Raphanel, J., Pure & Appl. Geophys., **166** (2009).
18. Brandt, H., ASME, J. Appl. Mech., **22** (1965).